

**PROCEEDINGS OF
THE ROYAL SOCIETY A**

MATHEMATICAL, PHYSICAL AND ENGINEERING SCIENCES

**Linear analysis of ice-shelf topography response to basal
melting and freezing**

Journal:	<i>Proceedings A</i>
Manuscript ID	Draft
Article Type:	Research
Date Submitted by the Author:	n/a
Complete List of Authors:	Stubblefield, Aaron; Dartmouth College, Thayer School of Engineering Wearing, Martin; The University of Edinburgh School of GeoSciences Meyer, Colin; Dartmouth College, Thayer School of Engineering
Subject:	Glaciology < EARTH SCIENCES, Fluid mechanics < PHYSICS
Keywords:	ice-shelf melting, ice-shelf freeze-on, ice-shelf channels, floating viscous sheets, secondary flow
Subject Category:	Earth Science

SCHOLARONE™
Manuscripts

1
2
3 **Author-supplied statements**
4

5 Relevant information will appear here if provided.
6

7
8 **Ethics**
9

10 *Does your article include research that required ethical approval or permits?:*

11 This article does not present research with ethical considerations
12

13 *Statement (if applicable):*

14 CUST_IF_YES_ETHICS :No data available.
15

16
17 **Data**
18

19 *It is a condition of publication that data, code and materials supporting your paper are made publicly*
20 *available. Does your paper present new data?:*

21 Yes
22

23 *Statement (if applicable):*

24 No new data are presented in this study. The code is openly available at
25 <https://github.com/agstub/linear-shelf-melt> (see Jupyter notebooks) and will be archived with
26 Zenodo prior to publication.
27

28
29 **Conflict of interest**
30

31 I/We declare we have no competing interests
32

33 *Statement (if applicable):*

34 CUST_STATE_CONFLICT :No data available.
35
36
37
38
39
40
41
42
43
44
45
46
47
48
49
50
51
52
53
54
55
56
57
58
59
60

PROCEEDINGS A

royalsocietypublishing.org/journal/rspa

Research



Article submitted to journal

Subject Areas:

glaciology, geophysics, mathematical modeling

Keywords:

ice-shelf melting, ice-shelf freeze-on, ice-shelf channels, floating viscous sheets, secondary flow

Author for correspondence:

A. G. Stubblefield

e-mail:

aaron.g.stubblefield@dartmouth.edu

Linear analysis of ice-shelf topography response to basal melting and freezing

A. G. Stubblefield¹, M. G. Wearing² and C. R. Meyer¹¹Thayer School of Engineering, Dartmouth College, Hanover, NH, USA²School of Geosciences, University of Edinburgh, Edinburgh, UK

Floating ice shelves in Antarctica and Greenland limit land-ice contributions to sea level rise by resisting the flow of grounded ice. Melting at the surface and base of ice shelves can lead to destabilisation by promoting thinning and fracturing. Basal melting often results in channelised features that manifest as surface topography due to buoyancy. The assumption of hydrostatic flotation commonly underlies estimates of basal melting rates. However, numerical simulations and ice-penetrating radar data have shown that narrow topographic features do not necessarily satisfy the local flotation condition. Here, we introduce a linearised model for ice-shelf topographic response to basal melting perturbations to quantify deviations from hydrostatic flotation and the stability of topography. While hydrostatic flotation is the dominant behaviour at wavelengths greater than the ice thickness, ice elevation anomalies diminish relative to the perfect flotation condition at smaller wavelengths. The linearised analysis shows that steady solutions are stable. However, we do not consider physical effects such as fracturing, which could lead to instability. We find a Green's function for one-dimensional steady-state solutions in the absence of background advection. We validate the linearised analysis by comparing numerical solutions to a nonlinear ice-flow model with steady-state solutions obtained via the Green's function.

1. Introduction

Ice shelves and floating ice tongues in Greenland and Antarctica slow ice-mass loss and land-ice contributions to sea level rise by buttressing the flow of grounded ice [1–4]. Subglacial outflow near grounding lines and warm seawater intrusions can cause localised melting at the base of ice shelves [5–8]. Topographic features that are elongated in one direction, commonly called ice-shelf channels, have been found on many ice shelves and arise from localised melting at the base [7,9]. These anomalous topographic features manifest at the ice-shelf surface due to buoyancy. Ice-shelf channels have been associated with a variety of features including rifts, subglacial outflow, persistent polynyas, and terracing of the basal surface [9–11]. While channel formation is driven by persistent plumes of buoyant water, the dynamics vary and are influenced by the plume source (i.e., oceanic or subglacial), the presence of heterogeneous surfaces, and ice deformation [7,12–15].

Although melting dominates the basal mass balance of most Antarctic ice shelves [16], altimetry, ice-penetrating radar, and numerical models have shown that many ice shelves have regions where water is freezing to the base [17–22]. Borehole drilling has shown that thick units of frozen-on marine ice exist beneath the Amery Ice Shelf [23–25] and the Ronne-Filchner Ice Shelf [26,27]. Marine ice can have different rheological properties than meteoric ice due to differences in crystal size and orientation as well as the presence of interstitial brine [28]. Marine ice has also been found within suture zones, boundaries within ice shelves that separate different flow units, and may contribute to the structural stability of ice shelves by impeding fracture propagation [29–33]. For these reasons, quantifying the mechanical effects of marine ice accretion and refining inferences from ice-shelf topography remain important areas of investigation.

The melting or freezing rate at the base of ice shelves can be estimated from surface observations under the assumptions that the ice is undergoing hydrostatic flotation and that the horizontal velocity is depth-independent. In this limit, the surface elevation of the ice shelf relative to sea level only depends on the ice thickness and the densities of ice and water. However, since ice flows like a viscous fluid over long time scales [34–36], deviatoric (bridging) stresses in the ice can lead to a non-hydrostatic state where the ice-surface elevation is diminished relative to the hydrostatic elevation [37–39]. Ice-penetrating radar data from the Fimbul Ice Shelf, East Antarctica, shows that narrow basal channels can be associated with diminished topographic anomalies [14]. Similarly, hydrostatic imbalance was found in the vicinity of a channel on the Getz Ice Shelf, West Antarctica, by comparing hydrostatic flotation thickness estimates with ice thickness obtained from radar profiles along NASA Operation IceBridge transects [40]. When hydrostatic balance is not satisfied exactly, the velocity is not depth-independent due to the presence of a secondary flow that balances the formation of basal channels. Deviation of the surface velocity and elevation from hydrostatic balance produces errors in melting-rate estimates that are based solely on surface observations [39,40].

Previous models of subglacial channels have been used to explore deviations from hydrostatic flotation [38,39], coupling with ocean physics [13,41–43], inclusion of viscoelastic effects [44, 45], and evolution of ice-shelf stratigraphy [46]. In a similar setting, a small-perturbation approximation of the Stokes equations has been used to model the evolution of crevasses in ice shelves over long time scales in relation to oceanic forcing [47,48]. While detailed analyses of Stokes-based perturbation models have been developed previously for grounded ice [49–52], similar analyses for floating ice shelves have not been developed beyond the model for crevasse evolution in a floating viscous medium that is undergoing extension [47].

Here, we develop a detailed linearised analysis of the ice-shelf topographic response to melting or freezing perturbations at the base. We derive a linearised model based on a small perturbation approximation of a fully nonlinear Stokes-flow model. We analyse the problem via a spectral decomposition, discussing in detail long-wavelength singularities that are similar to those found previously [47]. In particular, we show that solutions are well-defined despite the singularities. We quantify conditions under which ice-elevation anomalies approach perfect flotation as well as the stability of steady-state solutions. To test the validity of the small-perturbation approach,

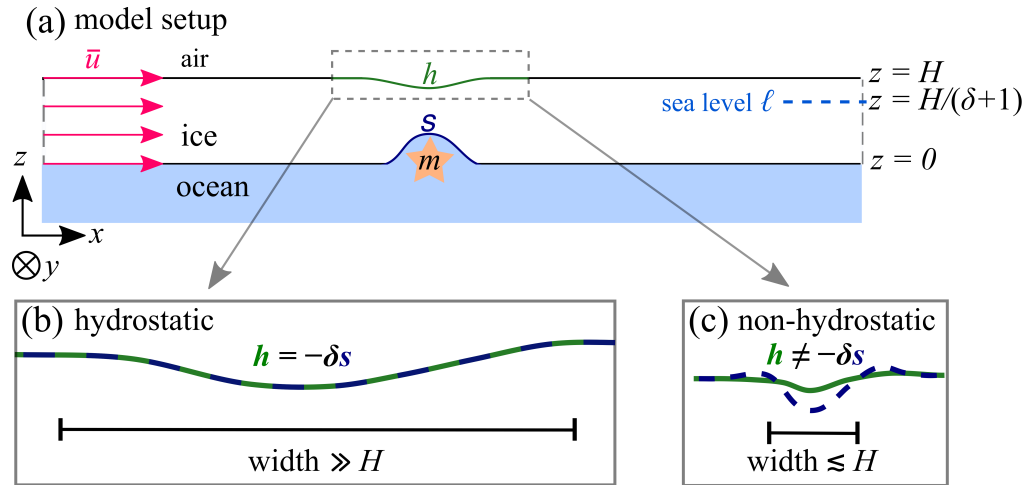


Figure 1. (a) Sketch of model variables. The ice-surface elevation perturbation is h , the elevation perturbation at the ice-water interface is s , the melting rate is m , the ice thickness is H , the sea level is ℓ , the flotation factor is $\delta = \rho_w / \rho_i - 1$, and advection from the background horizontal velocity is \bar{u} . The background flow (red arrows) is in the x direction, and the y direction points into the page. (b) Example of a topographic anomaly that is wide relative to the ice thickness and satisfies the perfect flotation condition ($h = -\delta s$) locally. (c) Example of a narrow topographic anomaly that does not satisfy the perfect flotation condition locally.

we compare numerical solutions obtained by solving the fully nonlinear ice-flow problem with a finite element method to semi-analytical steady-state solutions that we obtain with a Green's function. We conclude by discussing implications and avenues for further research.

2. Model derivation

(a) Governing equations

First, we outline a general Stokes model for ice-shelf flow. We assume that the domain is an ice shelf of finite thickness H and infinite horizontal extent (Figure 1a). The domain is defined by $|x| < \infty$, $|y| < \infty$, and $s \leq z \leq h$, where h and s are the upper and lower surfaces of the ice shelf, respectively. We assume that ice deforms according to the incompressible Stokes equations

$$-\nabla p + \nabla \cdot (2\eta \dot{\epsilon}) = \rho_i \mathbf{g} \quad (2.1)$$

$$\nabla \cdot \mathbf{u} = 0, \quad (2.2)$$

where $\mathbf{u} = [u, v, w]^T$ is the velocity, $\dot{\epsilon} = \frac{1}{2} (\nabla \mathbf{u} + \nabla \mathbf{u}^T)$ is the strain rate, η is the ice viscosity, p is the pressure, ρ_i is the ice density, and $\mathbf{g} = [0, 0, -g]^T$ is gravitational acceleration with magnitude g . We relate the ice viscosity to strain rate through a regularised Glen's flow law [34–36]

$$\eta = \frac{1}{2} B (|\dot{\epsilon}|^2 + \nu)^{\frac{1-n}{2n}}, \quad (2.3)$$

where n is the stress exponent, B is the ice hardness parameter, $|\dot{\epsilon}| = \sqrt{\frac{1}{2} \dot{\epsilon} : \dot{\epsilon}}$ is the second invariant, and ν is a regularization parameter that ensures finite viscosity in the limit of zero strain rate.

We assume a stress-free condition at the upper surface ($z = h$), which is equivalent to

$$[2\eta \dot{\epsilon} - p \mathbf{I}] \cdot \mathbf{n} = \mathbf{0}, \quad (2.4)$$

where \mathbf{n} is an upward-pointing unit normal to the ice boundary and \mathbf{I} is the identity tensor. The normal stress at the ice-water interface ($z = s$) is hydrostatic and the shear stress vanishes,

$$[2\eta\dot{\boldsymbol{\epsilon}} - p\mathbf{I}] \cdot \mathbf{n} = \rho_w g(\ell - s)\mathbf{n}, \quad (2.5)$$

where ρ_w is the water density and $z = \ell$ is the (far-field) sea level. Below, we set the sea level to $\ell = (\rho_i/\rho_w)H$, where H is the ice thickness in the uniform reference state.

The upper and lower surfaces of the ice shelf evolve according to kinematic equations that are coupled to the Stokes flow equations. The upper surface, $z = h(x, y, t)$, evolves according to

$$\frac{\partial h}{\partial t} + u \frac{\partial h}{\partial x} + v \frac{\partial h}{\partial y} = w + a, \quad (2.6)$$

where a denotes accumulation or ablation at the ice-shelf surface. Similarly, the lower surface, $z = s(x, y, t)$, evolves according to

$$\frac{\partial s}{\partial t} + u \frac{\partial s}{\partial x} + v \frac{\partial s}{\partial y} = w + m, \quad (2.7)$$

where m is the basal melting or freezing rate (Figure 1). We also require that all fields approach appropriate far-field reference states in the limits $|x| \rightarrow \infty$ and $|y| \rightarrow \infty$, which are naturally incorporated in the perturbation-based framework described below. While our focus is on a spectral analysis of the linearised problem, we also compare the results to solutions obtained by solving the fully nonlinear problem (2.1)-(2.7) with a finite element method, subject to additional boundary conditions on the side-walls of the computational domain.

(b) Perturbation equations

Next, we derive a linearisation of the problem (2.1)-(2.7). We take perturbations relative to a reference state characterised by uniform flow in the x direction, uniform ice thickness, cryostatic pressure, perfect flotation, and no surface accumulation or basal melting (Figure 1). Denoting the reference states with bars, these conditions are given by

$$\begin{aligned} \bar{u} \geq 0, \quad \bar{v} = 0, \quad \bar{w} = 0, \quad \bar{p} = \rho_i g(H - z), \quad \bar{\eta} = \frac{1}{2} B \nu^{\frac{1-n}{2n}}, \\ \bar{h} = H, \quad \bar{s} = 0, \quad \bar{\ell} = \frac{\rho_i}{\rho_w} H, \quad \bar{a} = 0, \quad \bar{m} = 0. \end{aligned} \quad (2.8)$$

We introduce small, localised perturbations (denoted by asterisks) to the reference states via

$$\begin{aligned} u = \bar{u} + \epsilon u_*, \quad v = \bar{v} + \epsilon v_*, \quad w = \bar{w} + \epsilon w_* \\ p = \bar{p} + \epsilon p_*, \quad s = \bar{s} + \epsilon s_*, \quad h = \bar{h} + \epsilon h_*, \quad m = \bar{m} + \epsilon m_*, \end{aligned} \quad (2.9)$$

where ϵ is a small parameter. For simplicity, we do not consider perturbations to the surface accumulation (or ablation) rate. We revisit possible sources of surface-mass balance perturbations and related model extensions in the discussion. We insert the perturbations (2.9) into (2.1)-(2.2) and discard the $O(\epsilon^2)$ terms to obtain a homogeneous, linear Stokes problem for the perturbed fields,

$$-\nabla p_* + \bar{\eta} \nabla^2 \mathbf{u}_* = \mathbf{0} \quad (2.10)$$

$$\nabla \cdot \mathbf{u}_* = 0. \quad (2.11)$$

Viscosity variations associated with Glen's flow law do not contribute to the first-order perturbation equations because the uniform-flow reference states have a strain rate of zero. Although not explored here, an extensional reference state results in a perturbation problem that depends on the stress exponent and background strain rates [47].

The surface kinematic equations (2.6) and (2.7) reduce to

$$\frac{\partial h_*}{\partial t} + \bar{u} \frac{\partial h_*}{\partial x} = w_* \quad (2.12)$$

$$\frac{\partial s_*}{\partial t} + \bar{u} \frac{\partial s_*}{\partial x} = w_* + m_* \quad (2.13)$$

To account for changes in ice geometry, we linearise the upper and lower surface boundary conditions at $z = H + h_*$ and $z = s_*$ onto $z = H$ and $z = 0$, respectively. The vanishing normal stress condition at $z = H + h_*$ in (2.4) is approximated at $z = H$ by

$$p_* - 2\bar{\eta} \frac{\partial w_*}{\partial z} = h_* \rho_i g \quad (2.14)$$

Similarly, the hydrostatic normal stress condition at the base in (2.5) becomes

$$p_* - 2\bar{\eta} \frac{\partial w_*}{\partial z} = -s_* \Delta \rho g \quad (2.15)$$

where $\Delta \rho = \rho_w - \rho_i$ is the density difference between ice and water. The vanishing shear-stress conditions in (2.4) and (2.5) take the form

$$\begin{aligned} \frac{\partial u_*}{\partial z} + \frac{\partial w_*}{\partial x} &= 0 \\ \frac{\partial v_*}{\partial z} + \frac{\partial w_*}{\partial y} &= 0 \end{aligned} \quad (2.16)$$

which hold at both the surface ($z = H$) and the base ($z = 0$). We drop the asterisk subscripts on the perturbed fields below.

A primary goal in the analysis below is to determine when the perfect flotation condition

$$h = -\delta s \quad (2.17)$$

is satisfied locally, where we have defined the flotation factor

$$\delta \equiv \frac{\rho_w}{\rho_i} - 1. \quad (2.18)$$

The perfect flotation condition (2.17) corresponds to a purely hydrostatic state (Figure 1b). However, deviatoric (bridging) stresses within the ice can support departures from this state [37–39](Figure 1c). While our analysis is focused on ice-shelf topography, testing whether or not the horizontal velocity is depth-independent is also possible in this framework.

(c) Fourier transform approach

We apply Fourier transforms with respect to the horizontal coordinates (x, y) to simplify the system (2.10)–(2.16). The Stokes equations (2.10)–(2.11), written component-wise, transform to

$$-ik_x \hat{p} + \bar{\eta} \left(-k^2 \hat{u} + \frac{\partial^2 \hat{u}}{\partial z^2} \right) = 0 \quad (2.19)$$

$$-ik_y \hat{p} + \bar{\eta} \left(-k^2 \hat{v} + \frac{\partial^2 \hat{v}}{\partial z^2} \right) = 0 \quad (2.20)$$

$$-\frac{\partial \hat{p}}{\partial z} + \bar{\eta} \left(-k^2 \hat{w} + \frac{\partial^2 \hat{w}}{\partial z^2} \right) = 0 \quad (2.21)$$

$$ik_x \hat{u} + ik_y \hat{v} + \frac{\partial \hat{w}}{\partial z} = 0, \quad (2.22)$$

where $\mathbf{k} = [k_x, k_y]^T$ is the horizontal wavevector with magnitude $k = \sqrt{k_x^2 + k_y^2}$. Equations (2.19)–(2.22) reduce to a fourth-order equation for the transformed vertical velocity [52],

$$\frac{\partial^4 \hat{w}}{\partial z^4} - 2k^2 \frac{\partial^2 \hat{w}}{\partial z^2} + k^4 \hat{w} = 0. \quad (2.23)$$

The general solution to (2.23) is

$$\hat{w} = \frac{c_1}{k} e^{kz} + \frac{c_2}{k} e^{-kz} + c_3 z e^{kz} + c_4 z e^{-kz}, \quad (2.24)$$

where the coefficients c_j depend on k . To determine the coefficients in (2.23), we rewrite all of the boundary conditions in terms of \hat{w} . The vanishing shear-stress conditions (2.16) along with the transformed incompressibility condition (2.22) imply that

$$\frac{\partial^2 \hat{w}}{\partial z^2} + k^2 \hat{w} = 0 \quad (2.25)$$

at $z = 0$ and $z = H$. The transformed normal-stress condition at the upper surface can be rewritten using (2.19)-(2.22) as

$$\bar{\eta} \left(3k^2 \frac{\partial \hat{w}}{\partial z} - \frac{\partial^3 \hat{w}}{\partial z^3} \right) = -k^2 \rho_i g \hat{h}, \quad (2.26)$$

and, similarly, the transformed normal-stress condition at the base becomes

$$\bar{\eta} \left(3k^2 \frac{\partial \hat{w}}{\partial z} - \frac{\partial^3 \hat{w}}{\partial z^3} \right) = k^2 \Delta \rho g \hat{s}. \quad (2.27)$$

We insert the formula for \hat{w} (2.24) into the boundary conditions (2.25)-(2.27) to obtain a linear system for the coefficients c_j ,

$$\begin{bmatrix} e^{k'} & -e^{-k'} & k' e^{k'} & -k' e^{-k'} \\ e^{k'} & e^{-k'} & (k' + 1) e^{k'} & (k' - 1) e^{-k'} \\ 1 & -1 & 0 & 0 \\ 1 & 1 & 1 & -1 \end{bmatrix} \begin{bmatrix} c_1 \\ c_2 \\ c_3 \\ c_4 \end{bmatrix} = \frac{\rho_i g}{2\bar{\eta}} \begin{bmatrix} -\hat{h} \\ 0 \\ \delta \hat{s} \\ 0 \end{bmatrix}, \quad (2.28)$$

where the scaled wavevector magnitude,

$$k' = kH, \quad (2.29)$$

appears due to evaluation of the boundary conditions at $z = H$.

We solve the linear system (2.28) for the coefficients c_j for all $k' > 0$. In the limit $k' \rightarrow 0$, the system is singular, meaning that the long-wavelength component of \hat{w} is not uniquely determined by the momentum balance alone. We show that solutions to the coupled problem are well-defined in the limit $k' \rightarrow 0$ because the surface evolution equations (2.12) and (2.13) impose additional constraints on the vertical velocity in relation to the surface elevations and melting rate. A necessary condition for the existence of solutions to (2.28) is that $\hat{h} \rightarrow -\delta \hat{s}$ as $k' \rightarrow 0$, or, equivalently,

$$\int_{-\infty}^{+\infty} \int_{-\infty}^{+\infty} h \, dx \, dy = - \int_{-\infty}^{+\infty} \int_{-\infty}^{+\infty} \delta s \, dx \, dy. \quad (2.30)$$

The condition (2.30) implies that the perturbations will satisfy the perfect flotation condition, $h = -\delta s$, on average, but not necessarily locally.

Substituting the coefficients c_j into (2.24), we obtain an expression for the vertical velocity at the upper surface,

$$\hat{w}|_{z=H} = -R\hat{h} - B\delta\hat{s}, \quad (2.31)$$

where the surface relaxation function R is given by

$$R = \frac{1}{t_r} \frac{e^{4k'} + 4k' e^{2k'} - 1}{k' [e^{4k'} - 2(1 + 2k'^2) e^{2k'} + 1]}, \quad (2.32)$$

and the buoyancy transfer function B is given by

$$B = \frac{1}{t_r} \frac{2(k' + 1) e^{3k'} + 2(k' - 1) e^{k'}}{k' [e^{4k'} - 2(1 + 2k'^2) e^{2k'} + 1]}. \quad (2.33)$$

In equations (2.32) and (2.33), we have introduced

$$t_r \equiv \frac{2\bar{\eta}}{\rho_i g H}, \quad (2.34)$$

which is the characteristic timescale for decay of surface topography in an infinitely thick viscous medium without buoyancy forcing [53]. In the analysis below, we compare the timescale t_r to a natural timescale that arises from competition between topographic relaxation and buoyancy.

Combining (2.12) and (2.31), the upper surface evolves according to

$$\frac{\partial \hat{h}}{\partial t} + [ik_x \bar{u} + R] \hat{h} = -B \delta \hat{s}. \quad (2.35)$$

Similarly, the vertical velocity at the lower surface is given by

$$\hat{w}|_{z=0} = -R \delta \hat{s} - B \hat{h}, \quad (2.36)$$

which, along with (2.13), leads to the evolution equation

$$\frac{\partial \hat{s}}{\partial t} + [ik_x \bar{u} + \delta R] \hat{s} = \hat{m} - B \hat{h}. \quad (2.37)$$

The relaxation function (2.32) and buoyancy function (2.33) are singular in the limit $k \rightarrow 0$ (Figure 2). Physically, these singularities imply that topographic relaxation and buoyancy adjustments occur instantaneously at long wavelengths under the assumption of an infinitely expansive ice shelf. Laurent expansions of R and B indicate that they grow like k^{-4} as $k \rightarrow 0$ in accordance with the similar crevasse evolution model [47]. Below, we will show that the asymptotic behaviour $R \sim B$ at long wavelengths is associated with a hydrostatic state because topographic relaxation is perfectly balanced by buoyancy. At short wavelengths, the behaviour $R \gg B$ can lead to diminished surface topography because the presence of deviatoric stresses causes the topographic relaxation to exceed the buoyancy forcing (Figure 2). For the purpose of computing the solutions below, we regularise the functions R and B (Appendix A). However, we show that the solutions are well-defined despite the singularities.

(d) Scaling

Now, we introduce a scaling for the model equations (2.35) and (2.37). We scale the variables according to

$$\begin{aligned} h &= H h', & s &= H s', & x &= H x', & k_x &= H^{-1} k'_x, & t &= t_r t', \\ R &= t_r^{-1} R', & B &= t_r^{-1} B', & m &= t_r^{-1} H m', \end{aligned} \quad (2.38)$$

where the viscous relaxation time scale t_r is defined in (2.34). Omitting primes, equations (2.35) and (2.37) become

$$\frac{\partial \hat{h}}{\partial t} + [ik_x \alpha + R] \hat{h} = -B \delta \hat{s} \quad (2.39)$$

$$\frac{\partial \hat{s}}{\partial t} + [ik_x \alpha + \delta R] \hat{s} = \hat{m} - B \hat{h}, \quad (2.40)$$

where the parameter

$$\alpha = \frac{\bar{u} t_r}{H} \quad (2.41)$$

is the background flow speed relative the the characteristic velocity scale H/t_r . Below, we show that solutions evolve over a longer time scale $t_e \equiv t_r \times 2(1 + \delta^{-1})$, which coincides with the characteristic time scale in shallow approximations of ice-shelf flow [54].

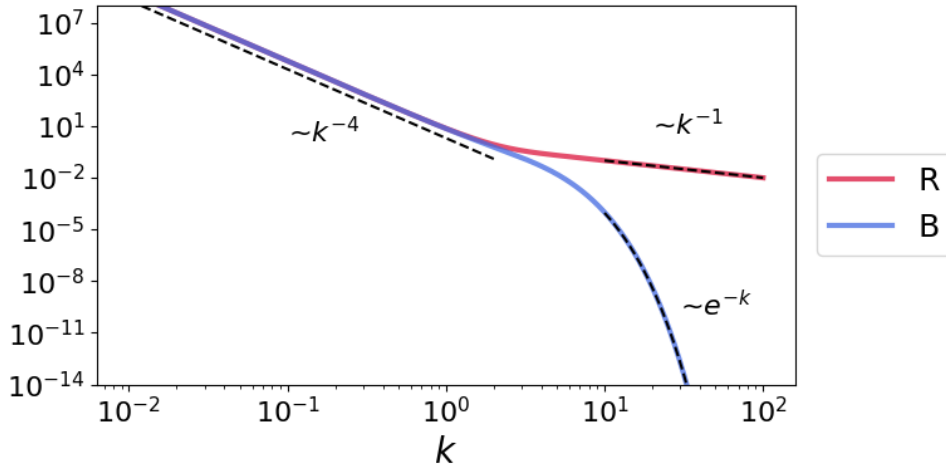


Figure 2. Graphs of R (2.32) and B (2.33) as functions of k (nondimensional), scaled by t_r^{-1} , along with their asymptotic behaviours as $k \rightarrow 0$ and $k \rightarrow \infty$ (dashed lines).

3. Analysis

Next, we derive and analyse general solutions to the problem (2.39)-(2.40) via a spectral decomposition. In particular, we quantify when solutions can be expected to deviate from the perfect flotation condition, $h = -\delta s$. We then derive steady solution formulas and find a Green's function for a one-dimensional melt channel in the absence of background advection ($\alpha = 0$). While our focus is on topography, velocity solutions can be derived and analysed once the elevations h and s are obtained. We provide expressions for the vertical and horizontal velocity solutions in Appendix B and C, respectively.

(a) General solutions

We rewrite the system (2.39)-(2.40) as

$$\frac{\partial \mathbf{y}}{\partial t} = \mathbf{A} \mathbf{y} + \mathbf{b}, \quad (3.1)$$

where

$$\mathbf{y} = \begin{bmatrix} \hat{h} \\ \hat{s} \end{bmatrix}, \quad \mathbf{b} = \begin{bmatrix} 0 \\ \hat{m} \end{bmatrix}, \quad \mathbf{A} = - \begin{bmatrix} ik_x \alpha + R & \delta B \\ B & ik_x \alpha + \delta R \end{bmatrix}. \quad (3.2)$$

To derive solutions and analyse their basic properties, we diagonalise the matrix \mathbf{A} according to

$$\mathbf{A} = \mathbf{P} \mathbf{D} \mathbf{P}^{-1}, \quad \mathbf{P} = \begin{bmatrix} | & | \\ \varphi_- & \varphi_+ \\ | & | \end{bmatrix}, \quad \mathbf{D} = \begin{bmatrix} \lambda_- & 0 \\ 0 & \lambda_+ \end{bmatrix}. \quad (3.3)$$

The eigenvalues (λ_{\pm}) and eigenvectors (φ_{\pm}) of \mathbf{A} in (3.3) are

$$\lambda_{\pm} = - \left(ik_x \alpha - \frac{\delta + 1}{2} R \mp \frac{\mu}{2} \right) \quad (3.4)$$

$$\varphi_{\pm} = \begin{bmatrix} \frac{R(1-\delta) \mp \mu}{2B} \\ 1 \end{bmatrix} \quad (3.5)$$

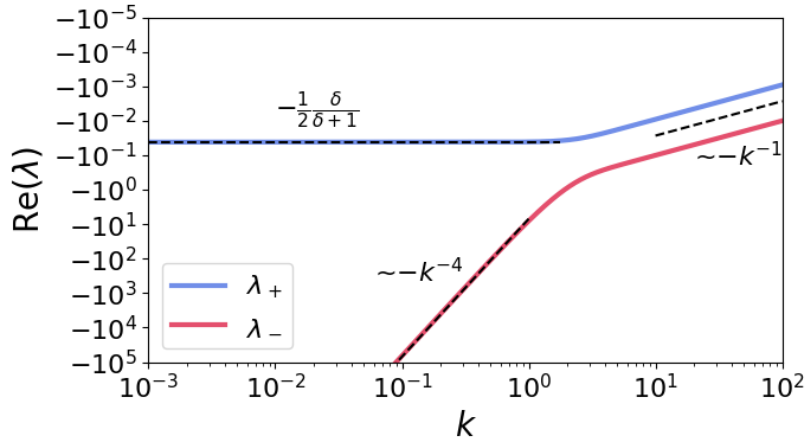


Figure 3. Real parts of the eigenvalues (λ_{\pm}) of \mathbf{A} along with their asymptotic behaviours as $k \rightarrow 0$ and $k \rightarrow \infty$ (dashed lines).

where we have defined

$$\mu = \sqrt{4\delta B^2 + R^2(\delta - 1)^2}. \quad (3.6)$$

The eigenvector corresponding to the dominant eigenvalue λ_+ has the limit $\varphi_+/\|\varphi_+\| \rightarrow [-\delta, 1]^T$ as $k \rightarrow 0$, which drives the solution towards the perfect flotation condition $h = -\delta s$ (Figure 3 and Figure 4). The other eigenpair encourages deviations from perfect flotation, but this effect decays as $k \rightarrow 0$ since λ_- becomes very negative (Figure 3). However, we show below that these effects can be important at short wavelengths. The normalised eigenvectors approach $\varphi_+/\|\varphi_+\| \rightarrow [0, 1]^T$ and $\varphi_-/\|\varphi_-\| \rightarrow [1, 0]^T$ as $k \rightarrow \infty$, meaning that the surface and basal responses becomes decoupled at short wavelengths because perturbations are not transmitted through the ice column.

Steady-state solutions are stable because the eigenvalues of \mathbf{A} have negative real part. Equation (3.4) implies that $\text{Re}(\lambda_-) < 0$ and $\text{Re}(\lambda_+) < 0$ if and only if $R > B$, which is satisfied for all $k > 0$ (Figure 2). However, other physics not considered here such as an extensional background state can lead to instability [47]. The long-wavelength limit of the dominant eigenvalue is

$$\lim_{k \rightarrow 0} \lambda_+ = -\frac{1}{2} \left(\frac{\delta}{\delta + 1} \right), \quad (3.7)$$

although this limit is approximately attained for $k \leq 1$ (Figure 3). This limit shows that solutions will tend to evolve over the longer timescale t_e defined by

$$t_e \equiv t_r \times 2 \left(1 + \frac{1}{\delta} \right) = \frac{4\eta}{\Delta\rho gH} \frac{\rho_w}{\rho_i}, \quad (3.8)$$

which is a characteristic timescale in shallow approximations of ice-shelf flow [54]. The timescale t_e (3.8) properly accounts for the competition between topographic relaxation and buoyancy in contrast to the original timescale t_r .

Assuming no initial perturbation, the solution to (3.1) is

$$\mathbf{y} = \int_0^t e^{\mathbf{A}(t-\tilde{t})} \mathbf{b}(\tilde{t}) d\tilde{t}, \quad (3.9)$$

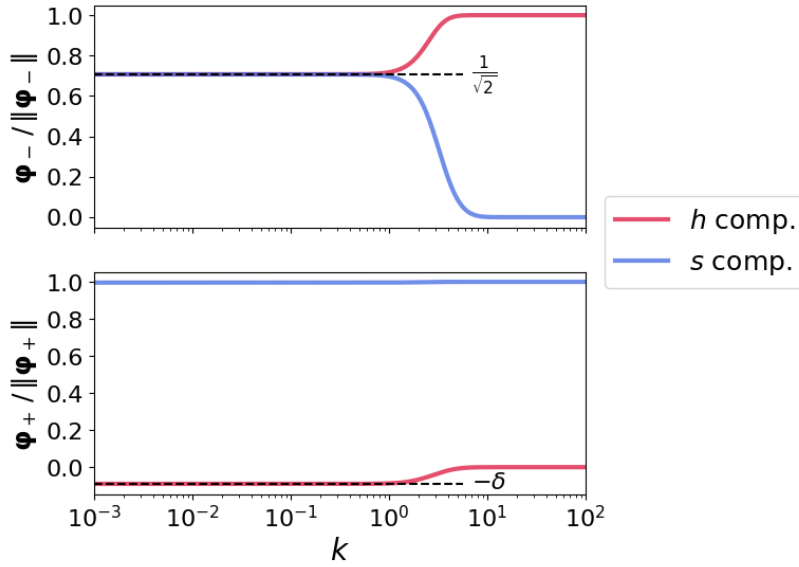


Figure 4. Normalised eigenvectors (φ_{\pm}) of \mathbf{A} . ‘ h comp.’ is the first vector component and ‘ s comp.’ is the second component in accordance with (3.2). Dashes lines highlight analytical limits.

where we compute the matrix exponential via $e^{\mathbf{A}t} = \mathbf{P}e^{\mathbf{D}t}\mathbf{P}^{-1}$. Equation (3.9) shows that the solution for the ice-surface elevation anomaly is

$$\begin{aligned}\hat{h} &= \int_0^t \mathbf{K}_h(t-\tilde{t})\hat{m}(\tilde{t})d\tilde{t}, \\ \mathbf{K}_h(t) &\equiv -\frac{\delta\mathbf{B}}{\mu}(e^{\lambda+t} - e^{\lambda-t}).\end{aligned}\quad (3.10)$$

Similarly, the solution for the elevation anomaly at the ice-water interface is

$$\begin{aligned}\hat{s} &= \int_0^t \mathbf{K}_s(t-\tilde{t})\hat{m}(\tilde{t})d\tilde{t}, \\ \mathbf{K}_s(t) &\equiv \frac{1}{2\mu}[(\mu + (1-\delta)\mathbf{R})e^{\lambda+t} + (\mu - (1-\delta)\mathbf{R})e^{\lambda-t}].\end{aligned}\quad (3.11)$$

The formulas (3.10) and (3.11) show that \hat{h} will be close to $-\delta\hat{s}$ provided that \mathbf{K}_h is close to $-\delta\mathbf{K}_s$ and $|\hat{m}|$ is not too large. We show the kernels \mathbf{K}_s and $-\mathbf{K}_h/\delta$ in Figure 5, highlighting that $\mathbf{K}_h(k, t) \approx -\delta\mathbf{K}_s(k, t)$ when $k \in (0, 1)$ and $t \in (10^{-1}, \infty)$. Therefore, significant deviations from perfect flotation only occur on fast timescales relative to the relaxation timescale or short wavelengths relative to the ice thickness. Finally, advection from the background flow, which is described by the α parameter, produces asymmetry and smaller surface perturbations. In the fast-flow limit ($\alpha \rightarrow \infty$), the perturbations decay to zero because the integral kernels in (3.10) and (3.11) become highly oscillatory due to the imaginary parts of the eigenvalues in (3.4). This limit occurs when the ice advects with the background flow too quickly to be disrupted by basal melting or freezing perturbations. We explore all of these effects in the examples below.

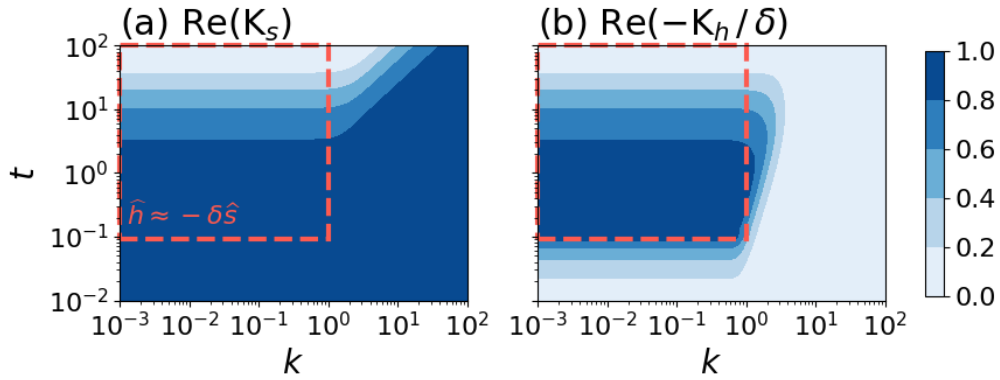


Figure 5. Real parts of the kernels K_s (3.11) and $-K_h/\delta$ (3.10) of the solution operators. The dashed boxes denote the region in (k, t) space where the flotation thickness is approximately satisfied since $K_h \approx -\delta K_s$.

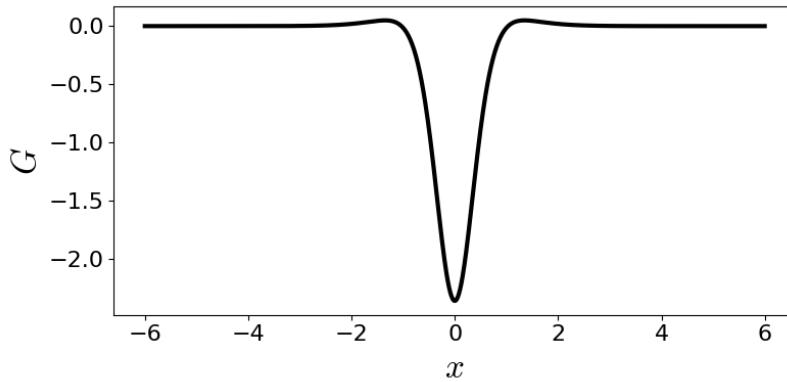


Figure 6. Graph of the free-space Green's function G given by equation (3.17).

(b) Steady states

We compute steady solutions via $[\hat{h}_e, \hat{s}_e]^T = -\mathbf{A}^{-1}\mathbf{b}$ to obtain

$$\hat{h}_e = -\frac{\delta B}{\delta(R^2 - B^2) + ik_x\alpha(\delta + 1)R - k_x^2\alpha^2} \hat{m} \quad (3.12)$$

$$\hat{s}_e = \frac{R + ik_x\alpha}{\delta(R^2 - B^2) + ik_x\alpha(\delta + 1)R - k_x^2\alpha^2} \hat{m}. \quad (3.13)$$

We derive a free-space Green's function for the steady problem assuming no background advection ($\alpha = 0$) and restricting the problem to one horizontal dimension (i.e., $k = |k_x|$). In the limit $\alpha \rightarrow 0$ we find

$$\hat{h}_e = \hat{G} \hat{m}_e. \quad (3.14)$$

where

$$\hat{G} \equiv -\frac{B}{R^2 - B^2} = -k^2 \coth(k) \operatorname{csch}(k) - k \operatorname{csch}(k). \quad (3.15)$$

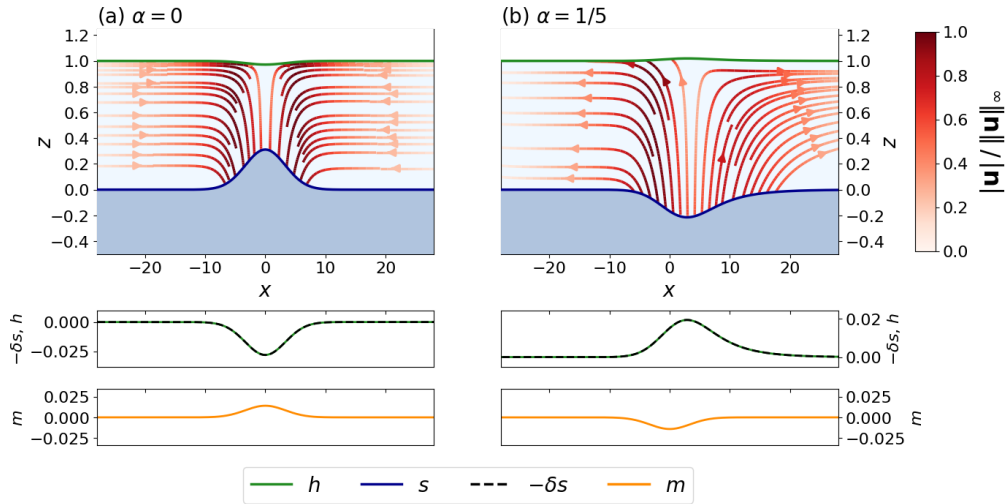


Figure 7. Steady ice-shelf profiles highlighting the flow field and topography. The profiles are taken along the $y = 0$ centerline. Normalised velocity streamlines are plotted on the deformed grid defined by $z \mapsto (1 - z)s + zh$. The elevation (green) and perfect flotation elevation $-\delta s$ (dashed black) are shown for each example, along with the melting or freezing rate m (orange). For both examples, the standard deviation of the melting rate is $\sigma = 10/3$.

Restricting the problem to one horizontal dimension (i.e., $k = |k_x|$), we use the convolution theorem to find the steady surface elevation via

$$h_e(x) = \int_{-\infty}^{+\infty} G(x - \tilde{x})m(\tilde{x}) d\tilde{x}, \quad (3.16)$$

where the free-space Green's function is

$$G(x) = \frac{\pi}{4} \operatorname{sech}^2\left(\frac{\pi x}{2}\right) \left[\pi x \tanh\left(\frac{\pi x}{2}\right) - 3 \right]. \quad (3.17)$$

In two horizontal dimensions, G corresponds to the steady elevation anomaly that arises when the melt rate is a line source (Figure 6).

4. Examples

Finally, we explore some steady-state solutions. In all of these examples, we choose a Gaussian-shaped melting or freezing anomaly that does not vary with time. Therefore, we set

$$m(x, y) = \pm m_0 \exp\left(-\frac{1}{2}(x^2 + y^2)/\sigma^2\right) \quad (4.1)$$

and choose an amplitude of $m_0 = 0.014$, which corresponds to a melt rate of 5 m/yr when $H = 500$ m, $\bar{\eta} = 10^{14}$ Pa s, and $\rho_i = 917$ kg/m³. In all examples, we set $\delta = 0.09$, which corresponds to a water density of $\rho_w = 1000$ kg/m³. We explore the effect of varying the advection parameter α , the width of the anomaly via σ , and the sign of the anomaly (Figures 7 and 8). We set either $\alpha = 0$ or $\alpha = 1/5$, corresponding to no background flow or a background flow of $\bar{u} \approx 77$ m/yr with the parameters cited above, respectively. We also show streamlines of the steady flow fields for each example. Expressions for the vertical and horizontal velocity fields are provided in Appendix B and Appendix C, respectively.

When the melting anomaly is wide relative to the ice thickness ($\sigma = 10/3$), we find that the steady surface elevation closely matches the perfect flotation condition (Figure 7a). Introducing background advection leads to asymmetry in the surfaces and flow fields (Figure 7b). We find

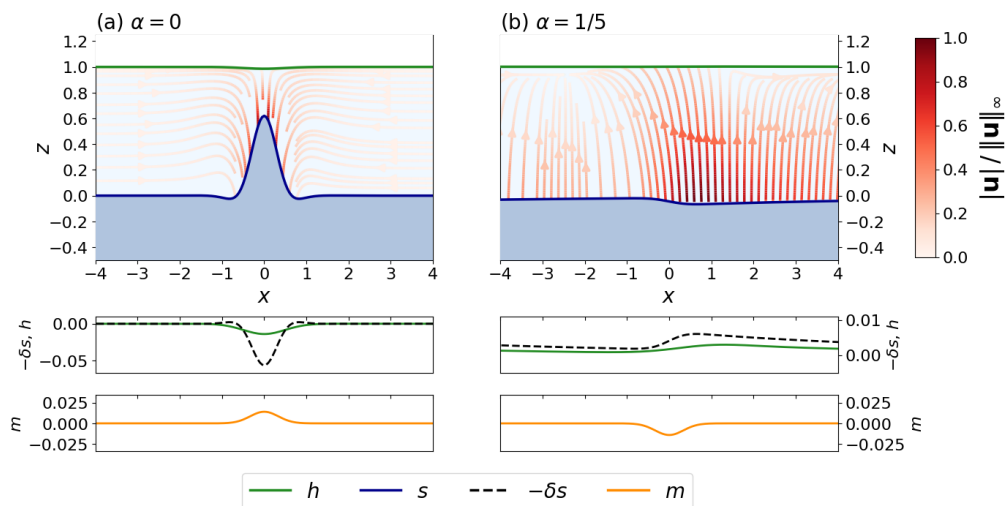


Figure 8. Same as Figure 7 except that the standard deviation of the melting rate is set to $\sigma = 1/3$. The ice-surface elevations (green lines) deviate from the perfect flotation condition (dashed lines).

that deviations from perfect flotation ($h \neq -\delta s$) occur when the melting anomaly width reaches the ice thickness ($\sigma = 1/3$) or smaller. In this regime, the elevation anomaly is diminished relative to the perfect flotation elevation (Figure 8a). At these smaller length scales, advection from the background flow produces pronounced asymmetry and the surface expression of the basal anomaly can be greatly diminished (Figure 8b).

We also compare the one-dimensional convolution solution (3.16) to a solution obtained by solving the fully nonlinear problem (2.1)-(2.7) with a finite element method [55]. In the flow law (2.3), we set the stress exponent to $n = 4$, the ice hardness to $B = 10 \times 10^8 \text{ Pa s}^{1/n}$ [56], and the viscosity regularization parameter ν to coincide with the background viscosity $\bar{\eta} = 10^{14} \text{ Pa s}$ at zero strain rate with these parameters. On the side-walls of the computational domain, we set the horizontal velocity and vertical shear stress to zero. We set the melting rate to be a one-dimensional Gaussian analogous to (4.1) with $y = 0$. The computational domain is defined by a height of $H = 500 \text{ m}$ and width of 40 km , which is discretised by a uniform mesh with an element width of 100 m . The sea level is set to $\ell = (\rho_i/\rho_w)H$ in the lower-surface boundary condition (2.5). The velocity and pressure are approximated by Taylor-Hood elements [55]. To allow for steady-state solutions in this confined setting, we set a constant accumulation rate a in (2.6) that is equal to the average melt rate [39]. We have implemented the finite element method in FEniCSx and made it openly available as described in the Data Availability section [57-59].

We find that the nonlinear solution reaches steady state by $t = 5 t_e$. For the parameters listed above, the finite element solution closely matches the Green's function solution (3.16) when the melt rate is small, e.g., 1 m/yr in dimensional terms (Figure 9a). When the melt rate is larger, there can be deviations between the Green's function solution and finite element solution due to nonlinearities in the original problem (2.1)-(2.7) and the lateral confinement in the numerical solution (Figure 9b). Deviations from an isoviscous state in the nonlinear model is controlled by the rheology parameters B and n in the flow law (2.3), which influence the agreement with the linearised model. Linearisation of the boundary conditions onto the simplified domain also contributes to the accuracy of the small-perturbation solutions when the channel incises through a significant fraction of the ice thickness (Figure 9b).

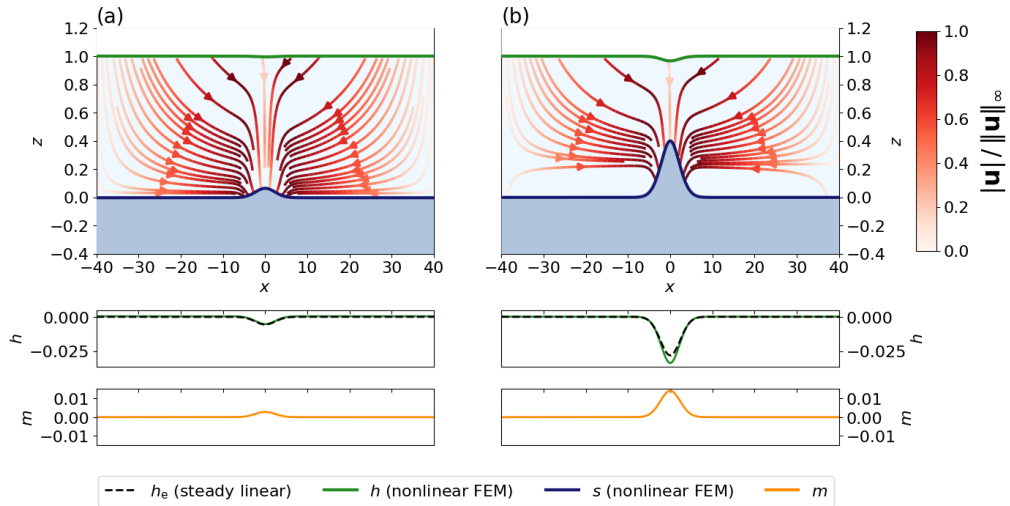


Figure 9. Nonlinear solutions obtained with a finite element method in one horizontal dimension for two different basal melting rates. The melting rate in panel (b) is five times larger than the melting rate in panel (a). The finite element solutions are shown at time $t = 5 t_e$ and have reached steady state. Steady state Green's function solutions h_e given by (3.16)-(3.17) are shown as dashed lines.

5. Discussion

The linearised analysis shows that short wavelength topography can deviate from perfect flotation even in steady state. These non-hydrostatic effects are due to the presence of non-negligible deviatoric (bridging) stresses. As the ice thickness is typically assumed to be in hydrostatic balance, non-hydrostatic effects can influence the accuracy basal melt-rate estimates [38–40]. For example, recent numerical modelling showed that the true melt rate and hydrostatic melt-rate estimate can have a pointwise mismatch of up to 25%, although the total effect was less than 1% when integrated over the entire domain [39]. Incorporating hydrostatic imbalance into estimates of ice thickness and discharge could help to sharpen melt-rate estimates. The linearised model developed herein could potentially be used to invert for the basal melt rate from altimetry data while allowing for hydrostatic imbalance. For example, equation (3.10) suggests that the inverse problem would take the form of a spatiotemporal deconvolution. Further validation against nonlinear models and comparison with existing estimation methods would be necessary steps in applying the linearised model to estimate basal melt rates.

Several nonlinear effects not considered in our analysis may also influence the evolution of melt-generated ice shelf topography. For example, ice deformation effects such as proximity to the grounding line [22,60], varying ice-shelf geometry, extensional stress regimes and fracture [47,48], or viscoelasticity [45] may produce different non-hydrostatic effects relative to the purely viscous shelves considered here. We have also assumed that the melting or freezing rate is a prescribed forcing function in this model. While considering non-hydrostatic effects can help to improve estimates of basal melting from surface observations, models that include oceanic physics coupled to ice deformation are needed to fully understand the physical processes governing ice-ocean interaction and predict the ice-shelf response to ocean warming [12,13,61–64]. Observations also suggest complex relations between ocean conditions, melting rate, and basal ice properties. For example, ice-penetrating radar and autonomous underwater vehicles have shown that melting depends on the ice roughness or slope of the ice-water interface [11,15,65]. Further modelling and analysis would be useful for elucidating the effects that these processes have on the evolution of ice-shelf topography that is generated by melting at the base.

In our linearised analysis, we excluded perturbations in ice-surface mass balance for simplicity. Localised changes in mass balance at the ice-shelf surface are often related to hydrology [66–70]. In particular, the drainage of ponded water on ice shelves can lead to flexure and potential instability [71–74]. For example, supraglacial lake drainage has been linked to the breakup of the Larsen B Ice Shelf [75,76]. As observations suggest that basal channels and surface hydrology can be coupled [77], implementing surface hydrology in ice-shelf models is a valuable avenue for future work [78,79]. While including surface mass balance perturbations in our linearised analysis is straightforward, we would need to modify our model so that the normal stress condition at the surface accounts for the load associated with ponded water and include additional physics to describe the redistribution of surface waters [80]. We could explore the effects of lateral variations in ice density due to variations in firn properties in a similar way [81]. We leave considerations of perturbations related to surface hydrology or ice density variations for future work.

Finally, the theory developed herein could potentially be extended to analyse the evolution of topography on icy satellites that are thought to have subsurface oceans, like Europa and Enceladus [82–84]. Our analysis diverges from previous treatments of icy satellite topography wherein pressure gradients are assumed to balance shear stresses similar to the shallow-ice approximation for land-based glaciers [85,86]. Further analysis of the physics governing topographic evolution on icy satellites and terrestrial ice shelves would be value for elucidating connections with subsurface thermomechanical processes at the ice-water interface [87,88].

6. Conclusions

Here, we have derived and analysed a linearised model for the evolution of ice-shelf topography that is generated by melting or freezing at the base. We derived a spectral decomposition of the linearised problem to elucidate the dominant modes and time scales governing channel evolution. The analysis shows that the flotation condition is the dominant mode at longer wavelengths, while shorter wavelength topography can persist in hydrostatic imbalance indefinitely. We illustrated through several examples the variety of topographic expressions that can result from a Gaussian-shaped melting rate when advection or the width of the anomaly are modified. We validated the linearised approach for the examples herein by comparing steady solutions obtained via a Green's function to solutions of the fully nonlinear problem obtained with a finite element method. Future work should focus on including hydrostatic imbalance in basal melting estimates, further constraining the ice-ocean interactions that lead to channel incision, and determining the influence that channelisation has on ice-shelf stability.

Data Accessibility. No new data are presented in this study. The code is openly available at <https://github.com/agstub/linear-shelf-melt> and will be archived with Zenodo prior to publication.

Authors' Contributions. A.G.S. conceived the study, developed the analysis, conducted numerical simulations, and drafted the manuscript. C.R.M. and M.G.W. provided valuable insight in the analysis and helped revise the manuscript.

Competing Interests. The authors declare no competing interests.

Acknowledgements. We thank Jonathan Kingslake and David Porter for discussions about the small-perturbation model.

Funding. A.G.S. was supported by NSF (2012958). C.R.M. was supported by NSF (2012958); ARO (78811EG); and NASA (80NSSC21M0329).

Appendix A. Regularisation

To remove the singularities in R and B for the purpose of computation, we define the regularised relaxation and buoyancy functions

$$R_\theta = (\theta + R^{-1})^{-1}, \quad B_\theta = (\theta + B^{-1})^{-1}, \quad (6.1)$$

where θ is a small regularisation parameter. We choose θ such that the analytical limit $R_\theta - B_\theta \rightarrow \frac{1}{4}$ as $k \rightarrow 0$ is attained at $k = 10^{-3}$, resulting in $\theta \approx 2.5 \times 10^{-14}$. The regularisation results in other analytical limits in the problem being respected at small k (Figure 3 and Figure 4). These regularisations are only used to facilitate computation of the solutions; we show in the main text that the solutions are well-defined without any regularisation. Analogous regularisations are employed for the velocity response functions derived in Appendix B and Appendix C.

Appendix B. Vertical velocity

Velocity solutions can be obtained after solving for the elevations h and s . The surface elevation equations remedy the singularity of the system (2.28) in the limit $k \rightarrow 0$ by determining the long-wavelength component. In steady state, equations (2.12) and (2.13) imply that the long-wavelength limits of the vertical velocity at the surface and base are

$$\lim_{k \rightarrow 0} \hat{w}|_{z=H} = 0, \quad \lim_{k \rightarrow 0} \hat{w}|_{z=0} = - \lim_{k \rightarrow 0} \hat{m}. \quad (6.2)$$

The elevation solutions derived in the main text result in these limits being satisfied in (2.31) and (2.36). We apply the limits (6.2) to (2.24) to find that the the long-wavelength component of the vertical velocity on the interior of the ice is

$$\lim_{k \rightarrow 0} \hat{w} = - \left(1 - \frac{z}{H}\right) \lim_{k \rightarrow 0} \hat{m}. \quad (6.3)$$

The particular expression for \hat{w} (2.24) at an arbitrary depth is given by

$$\hat{w} = -W_h \hat{h} - W_s \delta \hat{s}, \quad (6.4)$$

where the functions W_h and W_s are

$$W_h = \frac{1}{t_r} \left[\left(k' z' \left((2k' + 1) e^{2k'} - 1 \right) + k' + (k' + 1) e^{2k'} - \left(k' z' \left(2k' + e^{2k'} - 1 \right) - (k' + 1) e^{2k'} - k' + 1 \right) e^{2k' z'} - 1 \right) e^{k'(1-z')} \right] / L \quad (6.5)$$

$$W_s = \frac{1}{t_r} \left[\left(\left(k' z' \left((2k' + 1) e^{2k'} - 1 \right) - \left(2k'^2 + 2k' + 1 \right) e^{2k'} + 1 \right) e^{2k' z'} - \left(k' z' \left(2k' + e^{2k'} - 1 \right) - 2k'^2 + 2k' + e^{2k'} - 1 \right) e^{2k'} \right) e^{-k' z'} \right] / L \quad (6.6)$$

$$L = k' (e^{4k'} - 2(1 + 2k'^2) e^{2k'} + 1) \quad (6.7)$$

These response functions reduce to R and B when evaluated at the upper and lower surfaces in accordance with equations (2.31) and (2.36).

Appendix C. Horizontal velocity

We now outline a derivation of expressions for the horizontal velocities. We derive only the component in the x direction, u ; the derivation of the y component, v , is analogous except with k_x

replaced by k_y . The transformed horizontal momentum equation (2.19) has the general solution

$$\hat{u}(z) = \frac{ik_x}{2\eta k} \left[e^{kz} \int_0^z \hat{p}(\tilde{z}) e^{-k\tilde{z}} d\tilde{z} - e^{-kz} \int_0^z \hat{p}(\tilde{z}) e^{k\tilde{z}} d\tilde{z} \right] + d_1 e^{kz} + d_2 e^{-kz}, \quad (6.8)$$

where d_1 and d_2 depend on k . Using the identity $\hat{p} = \bar{\eta} (k^{-2} \hat{w}_{zzz} - \hat{w}_z)$, we find that equation (6.8) reduces to

$$\hat{u}(z) = \frac{ik_x}{k^2} P(z) + d_1 e^{kz} + d_2 e^{-kz} \quad (6.9)$$

$$P(z) = \hat{w}_z - \hat{w}_z|_{z=0} \cosh(kz) - \frac{1}{k} \hat{w}_{zz}|_{z=0} \sinh(kz). \quad (6.10)$$

Equation (6.9) and the vanishing shear-stress conditions, $\hat{u}_z = -ik_x \hat{w}$, at $z = H$ and $z = 0$ lead to the linear system

$$\begin{bmatrix} e^{k'} & -e^{-k'} \\ 1 & -1 \end{bmatrix} \begin{bmatrix} d_1 \\ d_2 \end{bmatrix} = -\frac{ik_x}{k^2} \begin{bmatrix} k\hat{w}|_{z=H} + \frac{1}{k} P_z(H) \\ k\hat{w}|_{z=0} \end{bmatrix}, \quad (6.11)$$

where $\hat{w}|_{z=H}$ and $\hat{w}|_{z=0}$ are given by (2.31) and (2.36), respectively. After solving the system (6.11) for the coefficients d_1 and d_2 , we can write the horizontal velocity in (6.9) as

$$\hat{u} = ik_x (U_h \hat{h} + U_s \delta \hat{s}), \quad (6.12)$$

where the response functions U_h and U_s are

$$U_h = \frac{1}{t_r} \left[z'((1 - 2k' - e^{2k'})e^{2k'z'} + 1) + (1 - z'(1 + 2k'))e^{2k'} + e^{2k'(z'+1)}(e^{2k'} - 1) - 1 \right] \times e^{k'(1-z')} / L \quad (6.13)$$

$$U_s = \frac{1}{t_r} \left[z'(e^{2k'z'} - e^{4k'} - (1 + 2k')e^{2k'(z'+1)}) + 2k'e^{2k'(z'+1)} + (-2k'z' + 2k' + z')e^{2k'} \right] \times e^{-k'z'} / L, \quad (6.14)$$

where L is defined in (6.7). As with the vertical velocity, the coupling with the elevation solutions renders the horizontal velocity well-defined in the limit $k \rightarrow 0$ even though the system (6.11) is singular. We find that that $\hat{u} \rightarrow 0$ as $k \rightarrow 0$ for the examples herein, which is the expected behavior for a symmetric flow field with vanishing horizontal integral.

References

1. Scambos TA, Bohlander J, Shuman CA, Skvarca P. 2004 Glacier acceleration and thinning after ice shelf collapse in the Larsen B embayment, Antarctica. *Geophysical Research Letters* **31**.
2. Paolo FS, Fricker HA, Padman L. 2015 Volume loss from Antarctic ice shelves is accelerating. *Science* **348**, 327–331.
3. Fürst JJ, Durand G, Gillet-Chaulet F, Tavard L, Rankl M, Braun M, Gagliardini O. 2016 The safety band of Antarctic ice shelves. *Nature Climate Change* **6**, 479–482.
4. Pegler SS. 2018 Marine ice sheet dynamics: the impacts of ice-shelf buttressing. *Journal of Fluid Mechanics* **857**, 605–647.
5. Rignot E, Steffen K. 2008 Channelized bottom melting and stability of floating ice shelves. *Geophysical Research Letters* **35**.
6. Joughin I, Alley RB. 2011 Stability of the West Antarctic ice sheet in a warming world. *Nature Geoscience* **4**, 506–513.
7. Alley KE, Scambos TA, Siegfried MR, Fricker HA. 2016 Impacts of warm water on Antarctic ice shelf stability through basal channel formation. *Nature Geoscience* **9**, 290–293.
8. Joughin I, Shapero D, Smith B, Dutrieux P, Barham M. 2021 Ice-shelf retreat drives recent Pine Island Glacier speedup. *Science Advances* **7**, eabg3080.
9. Alley KE, Scambos TA, Alley RB. 2023 The role of channelized basal melt in ice-shelf stability: recent progress and future priorities. *Annals of Glaciology* pp. 1–5.

10. Le Brocq AM, Ross N, Griggs JA, Bingham RG, Corr HF, Ferraccioli F, Jenkins A, Jordan TA, Payne AJ, Rippin DM et al.. 2013 Evidence from ice shelves for channelized meltwater flow beneath the Antarctic Ice Sheet. *Nature Geoscience* **6**, 945–948.
11. Dutrioux P, Stewart C, Jenkins A, Nicholls KW, Corr HF, Rignot E, Steffen K. 2014 Basal terraces on melting ice shelves. *Geophysical Research Letters* **41**, 5506–5513.
12. Gladish CV, Holland DM, Holland PR, Price SF. 2012 Ice-shelf basal channels in a coupled ice/ocean model. *Journal of Glaciology* **58**, 1227–1244.
13. Sergienko O. 2013 Basal channels on ice shelves. *Journal of Geophysical Research: Earth Surface* **118**, 1342–1355.
14. Langley K, Von Deschanden A, Kohler J, Sinisalo A, Matsuoka K, Hattermann T, Humbert A, Nøst O, Isaksson E. 2014 Complex network of channels beneath an Antarctic ice shelf. *Geophysical Research Letters* **41**, 1209–1215.
15. Schmidt BE, Washam P, Davis PE, Nicholls KW, Holland DM, Lawrence JD, Riverman KL, Smith JA, Spears A, Dichek D et al.. 2023 Heterogeneous melting near the Thwaites Glacier grounding line. *Nature* **614**, 471–478.
16. Rignot E, Jacobs S, Mouginot J, Scheuchl B. 2013 Ice-shelf melting around Antarctica. *Science* **341**, 266–270.
17. Thomas RH. 1979 Ice shelves: a review. *Journal of Glaciology* **24**, 273–286.
18. Fricker HA, Popov S, Allison I, Young N. 2001 Distribution of marine ice beneath the Amery Ice Shelf. *Geophysical Research Letters* **28**, 2241–2244.
19. Joughin I, Padman L. 2003 Melting and freezing beneath Filchner-Ronne Ice Shelf, Antarctica. *Geophysical Research Letters* **30**.
20. Holland PR, Corr HF, Vaughan DG, Jenkins A, Skvarca P. 2009 Marine ice in Larsen ice shelf. *Geophysical Research Letters* **36**.
21. Galton-Fenzi B, Hunter J, Coleman R, Marsland S, Warner R. 2012 Modeling the basal melting and marine ice accretion of the Amery Ice Shelf. *Journal of Geophysical Research: Oceans* **117**.
22. Whiteford A, Horgan H, Leong W, Forbes M. 2022 Melting and refreezing in an ice shelf basal channel at the grounding line of the Kamb Ice Stream, West Antarctica. *Journal of Geophysical Research: Earth Surface* **127**, e2021JF006532.
23. Craven M, Allison I, Brand R, Elcheikh A, Hunter J, Hemer M, Donoghue S. 2004 Initial borehole results from the Amery Ice Shelf hot-water drilling project. *Annals of Glaciology* **39**, 531–539.
24. Craven M, Carsey F, Behar A, Matthews J, Brand R, Elcheikh A, Hall S, Treverrow A. 2005 Borehole imagery of meteoric and marine ice layers in the Amery Ice Shelf, East Antarctica. *Journal of Glaciology* **51**, 75–84.
25. Craven M, Allison I, Fricker HA, Warner R. 2009 Properties of a marine ice layer under the Amery Ice Shelf, East Antarctica. *Journal of Glaciology* **55**, 717–728.
26. Engelhardt H, Determann J. 1987 Borehole evidence for a thick layer of basal ice in the central Ronne Ice Shelf. *Nature* **327**, 318–319.
27. Oerter H, Kipfstuhl J, Determann J, Miller H, Wagenbach D, Minikin A, Graft W. 1992 Evidence for basal marine ice in the Filchner–Ronne Ice Shelf. *Nature* **358**, 399–401.
28. Treverrow A, Warner RC, Budd WE, Craven M. 2010 Meteoric and marine ice crystal orientation fabrics from the Amery Ice Shelf, East Antarctica. *Journal of Glaciology* **56**, 877–890.
29. Jansen D, Luckman A, Kulesa B, Holland PR, King EC. 2013 Marine ice formation in a suture zone on the Larsen C Ice Shelf and its influence on ice shelf dynamics. *Journal of Geophysical Research: Earth Surface* **118**, 1628–1640.
30. Kulesa B, Jansen D, Luckman AJ, King EC, Sammonds PR. 2014 Marine ice regulates the future stability of a large Antarctic ice shelf. *Nature communications* **5**, 3707.
31. McGrath D, Steffen K, Holland PR, Scambos T, Rajaram H, Abdalati W, Rignot E. 2014 The structure and effect of suture zones in the Larsen C Ice Shelf, Antarctica. *Journal of Geophysical Research: Earth Surface* **119**, 588–602.
32. Kulesa B, Booth AD, O’Leary M, McGrath D, King EC, Luckman AJ, Holland PR, Jansen D, Bevan SL, Thompson SS et al.. 2019 Seawater softening of suture zones inhibits fracture propagation in Antarctic ice shelves. *Nature Communications* **10**, 5491.
33. Larour E, Rignot E, Poinelli M, Scheuchl B. 2021 Physical processes controlling the rifting of Larsen C Ice Shelf, Antarctica, prior to the calving of iceberg A68. *Proceedings of the National Academy of Sciences* **118**, e2105080118.
34. Glen JW. 1955 The creep of polycrystalline ice. *Proceedings of the Royal Society of London. Series A. Mathematical and Physical Sciences* **228**, 519–538.

35. Greve R, Blatter H. 2009 *Dynamics of ice sheets and glaciers*. Springer Science & Business Media.
36. Cuffey KM, Paterson WSB. 2010 *The physics of glaciers*. Academic Press.
37. Van Der Veen CJ, Whillans I. 1989 Force budget: I. Theory and numerical methods. *Journal of Glaciology* **35**, 53–60.
38. Drews R. 2015 Evolution of ice-shelf channels in Antarctic ice shelves. *The Cryosphere* **9**, 1169–1181.
39. Wearing M, Stevens L, Dutriex P, Kingslake J. 2021 Ice-shelf basal melt channels stabilized by secondary flow. *Geophysical Research Letters* **48**, e2021GL094872.
40. Chartrand A, Howat I. 2020 Basal channel evolution on the Getz Ice Shelf, West Antarctica. *Journal of Geophysical Research: Earth Surface* **125**, e2019JF005293.
41. Millgate T, Holland PR, Jenkins A, Johnson HL. 2013 The effect of basal channels on oceanic ice-shelf melting. *Journal of Geophysical Research: Oceans* **118**, 6951–6964.
42. Sergienko O, Goldberg D, Little C. 2013 Alternative ice shelf equilibria determined by ocean environment. *Journal of Geophysical Research: Earth Surface* **118**, 970–981.
43. Dallaston M, Hewitt I, Wells A. 2015 Channelization of plumes beneath ice shelves. *Journal of Fluid Mechanics* **785**, 109–134.
44. Humbert A, Steinhage D, Helm V, Hoerz S, Berendt J, Leipprand E, Christmann J, Plate C, Müller R. 2015 On the link between surface and basal structures of the Jelbart Ice Shelf, Antarctica. *Journal of Glaciology* **61**, 975–986.
45. Humbert A, Christmann J, Corr HF, Helm V, Höyns LS, Hofstede C, Müller R, Neckel N, Nicholls KW, Schultz T et al.. 2022 On the evolution of an ice shelf melt channel at the base of Filchner Ice Shelf, from observations and viscoelastic modeling. *The Cryosphere* **16**, 4107–4139.
46. Drews R, Schannwell C, Ehlers T, Gladstone R, Pattyn F, Matsuoka K. 2020 Atmospheric and oceanographic signatures in the ice shelf channel morphology of Roi Baudouin Ice Shelf, East Antarctica, inferred from radar data. *Journal of Geophysical Research: Earth Surface* **125**, e2020JF005587.
47. Bassis JN, Ma Y. 2015 Evolution of basal crevasses links ice shelf stability to ocean forcing. *Earth and Planetary Science Letters* **409**, 203–211.
48. Kachuck SB, Whitcomb M, Bassis JN, Martin DF, Price SF. 2022 Simulating ice-shelf extent using damage mechanics. *Journal of Glaciology* **68**, 987–998.
49. Budd W. 1970 Ice flow over bedrock perturbations. *Journal of Glaciology* **9**, 29–48.
50. Hutter K, Legerer F, Spring U. 1981 First-order stresses and deformations in glaciers and ice sheets. *Journal of Glaciology* **27**, 227–270.
51. Balise MJ, Raymond CF. 1985 Transfer of basal sliding variations to the surface of a linearly viscous glacier. *Journal of Glaciology* **31**, 308–318.
52. Gudmundsson GH. 2003 Transmission of basal variability to a glacier surface. *Journal of Geophysical Research: Solid Earth* **108**.
53. Turcotte DL, Schubert G. 2002 *Geodynamics*. Cambridge university press.
54. Pegler SS, Worster MG. 2012 Dynamics of a viscous layer flowing radially over an inviscid ocean. *Journal of Fluid Mechanics* **696**, 152–174.
55. Stubblefield AG, Spiegelman M, Creyts TT. 2021 Variational formulation of marine ice-sheet and subglacial-lake grounding-line dynamics. *Journal of Fluid Mechanics* **919**, A23.
56. Millstein JD, Minchew BM, Pegler SS. 2022 Ice viscosity is more sensitive to stress than commonly assumed. *Communications Earth & Environment* **3**, 57.
57. Alnæs MS, Logg A, Ølgaard KB, Rognes ME, Wells GN. 2014 Unified Form Language: A Domain-Specific Language for Weak Formulations of Partial Differential Equations. *ACM Trans. Math. Softw.* **40**. ([10.1145/2566630](https://doi.org/10.1145/2566630))
58. Scroggs MW, Dokken JS, Richardson CN, Wells GN. 2022a Construction of Arbitrary Order Finite Element Degree-of-Freedom Maps on Polygonal and Polyhedral Cell Meshes. *ACM Trans. Math. Softw.* **48**. ([10.1145/3524456](https://doi.org/10.1145/3524456))
59. Scroggs MW, Baratta IA, Richardson CN, Wells GN. 2022b Basix: a runtime finite element basis evaluation library. *Journal of Open Source Software* **7**, 3982. ([10.21105/joss.03982](https://doi.org/10.21105/joss.03982))
60. Marsh OJ, Fricker HA, Siegfried MR, Christianson K, Nicholls KW, Corr HF, Catania G. 2016 High basal melting forming a channel at the grounding line of Ross Ice Shelf, Antarctica. *Geophysical Research Letters* **43**, 250–255.
61. Mueller R, Padman L, Dinniman MS, Erofeeva S, Fricker HA, King M. 2012 Impact of tide-topography interactions on basal melting of Larsen C Ice Shelf, Antarctica. *Journal of Geophysical Research: Oceans* **117**.

62. Washam P, Nicholls KW, Münchow A, Padman L. 2020 Tidal modulation of buoyant flow and basal melt beneath Petermann Gletscher Ice Shelf, Greenland. *Journal of Geophysical Research: Oceans* **125**, e2020JC016427.
63. Bradley AT, Rosie Williams C, Jenkins A, Arthern R. 2022 Asymptotic analysis of subglacial plumes in stratified environments. *Proceedings of the Royal Society A* **478**, 20210846.
64. Richter O, Gwyther DE, King MA, Galton-Fenzi BK. 2022 The impact of tides on Antarctic ice shelf melting. *The Cryosphere* **16**, 1409–1429.
65. Watkins RH, Bassis JN, Thouless M. 2021 Roughness of ice shelves is correlated with basal melt rates. *Geophysical Research Letters* **48**, e2021GL094743.
66. Bell RE, Chu W, Kingslake J, Das I, Tedesco M, Tinto KJ, Zappa CJ, Frezzotti M, Boghosian A, Lee WS. 2017 Antarctic ice shelf potentially stabilized by export of meltwater in surface river. *Nature* **544**, 344–348.
67. Kingslake J, Ely JC, Das I, Bell RE. 2017 Widespread movement of meltwater onto and across Antarctic ice shelves. *Nature* **544**, 349–352.
68. Bell RE, Banwell AF, Trusel LD, Kingslake J. 2018 Antarctic surface hydrology and impacts on ice-sheet mass balance. *Nature Climate Change* **8**, 1044–1052.
69. MacDonald GJ, Banwell AF, Willis IC, Mayer DP, Goodsell B, MacAYEAL DR. 2019 Formation of pedestalled, relict lakes on the McMurdo Ice Shelf, Antarctica. *Journal of Glaciology* **65**, 337–343.
70. Spergel JJ, Kingslake J, Creyts T, van Wessem M, Fricker HA. 2021 Surface meltwater drainage and ponding on Amery Ice Shelf, East Antarctica, 1973–2019. *Journal of Glaciology* **67**, 985–998.
71. Banwell AF, Macayeal DR. 2015 Ice-shelf fracture due to viscoelastic flexure stress induced by fill/drain cycles of supraglacial lakes. *Antarctic Science* **27**, 587–597.
72. MacAYEAL DR, Sergienko OV, Banwell AF. 2015 A model of viscoelastic ice-shelf flexure. *Journal of Glaciology* **61**, 635–645.
73. Banwell AF, Willis IC, Macdonald GJ, Goodsell B, MacAyeal DR. 2019 Direct measurements of ice-shelf flexure caused by surface meltwater ponding and drainage. *Nature communications* **10**, 730.
74. Arthur JF, Stokes CR, Jamieson SS, Carr JR, Leeson AA. 2020 Distribution and seasonal evolution of supraglacial lakes on Shackleton Ice Shelf, East Antarctica. *The Cryosphere* **14**, 4103–4120.
75. Banwell AF, MacAyeal DR, Sergienko OV. 2013 Breakup of the Larsen B Ice Shelf triggered by chain reaction drainage of supraglacial lakes. *Geophysical Research Letters* **40**, 5872–5876.
76. Leeson A, Forster E, Rice A, Gourmelen N, Van Wessem J. 2020 Evolution of supraglacial lakes on the Larsen B ice shelf in the decades before it collapsed. *Geophysical Research Letters* **47**, e2019GL085591.
77. Dow CF, Lee WS, Greenbaum JS, Greene CA, Blankenship DD, Poinar K, Forrest AL, Young DA, Zappa CJ. 2018 Basal channels drive active surface hydrology and transverse ice shelf fracture. *Science Advances* **4**, eaao7212.
78. Buzzard S, Feltham D, Flocco D. 2018a A mathematical model of melt lake development on an ice shelf. *Journal of Advances in Modeling Earth Systems* **10**, 262–283.
79. Buzzard S, Feltham D, Flocco D. 2018b Modelling the fate of surface melt on the Larsen C Ice Shelf. *The Cryosphere* **12**, 3565–3575.
80. Schoof C, Cook S, Kulesa B, Thompson S. 2023 The drainage of glacier and ice sheet surface lakes. *Journal of Fluid Mechanics* **961**, A4.
81. Holland PR, Corr HF, Pritchard HD, Vaughan DG, Arthern RJ, Jenkins A, Tedesco M. 2011 The air content of Larsen ice shelf. *Geophysical Research Letters* **38**.
82. Carr MH, Belton MJ, Chapman CR, Davies ME, Geissler P, Greenberg R, McEwen AS, Tufts BR, Greeley R, Sullivan R et al.. 1998 Evidence for a subsurface ocean on Europa. *Nature* **391**, 363–365.
83. Pappalardo RT, Belton MJ, Breneman H, Carr M, Chapman CR, Collins G, Denk T, Fagents S, Geissler PE, Giese B et al.. 1999 Does Europa have a subsurface ocean? Evaluation of the geological evidence. *Journal of Geophysical Research: Planets* **104**, 24015–24055.
84. Nimmo F, Pappalardo RT. 2016 Ocean worlds in the outer solar system. *Journal of Geophysical Research: Planets* **121**, 1378–1399.
85. Nye JF. 1952 The mechanics of glacier flow. *Journal of Glaciology* **2**, 82–93.
86. Nimmo F. 2004 Non-Newtonian topographic relaxation on Europa. *Icarus* **168**, 205–208.
87. Buffo J, Schmidt B, Huber C, Meyer C. 2021a Characterizing the ice-ocean interface of icy worlds: A theoretical approach. *Icarus* **360**, 114318.

- 1
2
3 88. Buffo J, Meyer C, Parkinson J. 2021b Dynamics of a solidifying icy satellite shell. *Journal of*
4 *Geophysical Research: Planets* **126**, e2020JE006741.
5
6
7
8
9
10
11
12
13
14
15
16
17
18
19
20
21
22
23
24
25
26
27
28
29
30
31
32
33
34
35
36
37
38
39
40
41
42
43
44
45
46
47
48
49
50
51
52
53
54
55
56
57
58
59

For Review Only